ORNL/TM-6354

Two- and Three-Dimensional Neutronics Calculations for the TFTR Neutral Beam Injectors

R. T. Santoro
R. A. Lillie
R. G. Alsmiller, Jr.
J. M. Barnes

OAK RIDGE NATIONAL LABORATORY
OPERATED BY UNION CARBIDE CORPORATION · FOR THE DEPARTMENT OF ENERGY

DISCLAIMER

Printed in the United States of America. Available from
National Technical Information Service
U.S. Department of Commerce
5285 Port Royal Road, Springfield, Virginia 22161
Price: Printed Copy $5.25; Microfiche $3.00

ORNL/TM-6354
Dist. Category UC-20d

Contract No. W-7405-eng-26

Engineering Physics Division

Two- and Three-Dimensional Neutronics Calculations for the TFTR Neutral Beam Injectors*

R. T. Santoro
R. A. Lillie
R. G. Alsmiller, Jr.
J. M. Barnes†

October, 1978

*Submitted for Journal publication

†Computer Sciences Division

OAK RIDGE NATIONAL LABORATORY
Oak Ridge, Tennessee 37830
operated by
UNION CARBIDE CORPORATION
for the
DEPARTMENT OF ENERGY

THIS PAGE

WAS INTENTIONALLY

LEFT BLANK

ACKNOWLEDGEMENTS

The authors wish to thank R. Little, G. Sheffield, H. J. Howe, Jr. and Long-poe Ku of Princeton Plasma Physics Laboratory and R. Hensler of Ebasco Services, Inc. for many helpful discussions and comments concerning these calculations. We also thank Margaret B. Emmett for her assistance in setting up the MORSE analysis code and R. L. Childs for his suggestions and advice in adapting the GRTUNCL computer code for the two-dimensional analysis.

THIS PAGE

WAS INTENTIONALLY

LEFT BLANK

ABSTRACT

Two- and three-dimensional radiation transport methods have been employed to estimate the nuclear performance of the neutral beam injectors being designed for the Tokamak Fusion Test Reactor. The nuclear heating rates and neutron and gamma-ray energy spectra have been calculated at various locations in a detailed calculational model of the injector using Monte Carlo methods. Calculations have also been carried out using discrete ordinates methods to obtain estimates of these data in a two-dimensional model of the injector. The two-dimensional calculational procedure was developed as an analytic tool for more cost efficient scoping and parametric studies of the effects of design changes on the injector performance due to the streaming of 14 MeV neutrons. The nuclear responses and spectra obtained using the two-dimensional calculational model agree with the more definitive data obtained using the three-dimensional model within approximately a factor of five.

I. INTRODUCTION

The Tokamak Fusion Test Reactor (TFTR) under construction at Princeton University represents a major commitment in the demonstration of fusion derived energy by magnetic confinement. The D-T fusion reactions will be initiated by the injection of neutral deuterium into a magnetically confined tritium plasma. The deuterons are energized and then neutralized in neutral beam injectors[1] and directed into the reactor through ducts that extend from the injector through a concrete, pillbox-shaped shield, referred to as the igloo, that surrounds the reactor. Inside the plasma, the deuterons collide with the tritons and electrons and, in the exchange of energy, heat the plasma. The deuterons also react with the tritons to form 14 MeV neutrons through the following reaction

$$D + T \rightarrow n + {}^{4}He + 17.6\ MeV.$$

Some of the neutrons formed in these reactions will stream through the injection ducts and interact in the injector components producing heat and other detrimental nuclear responses. Some of the neutrons will also impinge on the igloo wall and along with the secondary gamma rays produced by the neutron reactions in the concrete, leak through the shield and also contribute to the nuclear effects. The magnitude of the nuclear responses will impact the design, operation, and maintenance criteria for the neutral beam injectors.

This paper summarizes the results of two- and three-dimensional neutronics calculations that were carried out to aid in the design of the TFTR neutral beam injectors. The purpose of this study was to obtain the spatial dependences of the nuclear heating rates and the neutron and

gamma-ray scalar flux distributions at various locations in the neutral beam injector. The reason for using two radiation transport methods was to obtain a two-dimensional model for the injector which estimates the nuclear responses consistently with the more detailed three-dimensional analysis. Therefore, any future calculations to assess design changes, shielding requirements, or other nuclear responses could be more readily performed using the two-dimensional analysis.

The three-dimensional radiation transport calculations were carried out using the Monte Carlo code MORSE[2]. The nuclear responses were estimated at several locations in the injector using a detailed representation of the neutral beam injector and accurate energy, spatial, and angular distributions for the neutrons and gamma rays incident on the injector. However, in Monte Carlo calculations, the nuclear heating and scalar flux distributions may be estimated only at discrete locations in the injector and the number of these are limited by computer running time and cost constraints. The two-dimensional radiation transport calculations were carried out using the discrete-ordinates code DOT[3]. In this code, the nuclear responses may be obtained at all spatial locations in the grid mesh used to model the injector, but the injector model and the radiation source used to describe the radiation incident on the injector are more approximate than those used in the three-dimensional analysis.

A description of the neutral beam injector and the calculational models used in the two- and three-dimensional calculations are given in Section II. Also included are the details of the calculational procedures used to obtain the neutron and gamma-ray distributions incident on the injector. The results are presented and discussed in Section III.

II. INJECTOR MODELS AND DETAILS OF THE CALCULATIONS

A. Neutral Beam Injector Models

The operation of the neutral beam injector and the functions of its components are described in detail elsewhere[1,4-6], so only those features of the system necessary for this work and for describing the two- and three-dimensional injector models used in these calculations are given. The deuterium will be injected into the TFTR using four neutral beam lines positioned about the torus as shown in Fig. 1a. The axis of injection of each beam is approximately tangent to the toroidal axis of the reactor and passes through the igloo wall and into the torus between the toroidal field coils.

An elevation view of one of the injectors showing its location relative to the igloo shield and the TFTR is shown in Fig. 1b. The neutral beam injector components are housed in an $\sim$ 50 m^3 box-shaped vacuum vessel constructed primarily of stainless steel type-316 (SS-316). The inner vertical walls of the vessel are lined with cryocondensation vacuum pumping panels having a total active pumping area of 29.5 m^2 and have the capability for maintaining the injector vacuum at $\leq$ 3 x 10^{-3} torr. The vacuum enclosure contains three deuteron sources and ion neutralizing tubes that are mounted in an arc in the plane parallel to the plane of the floor. Each source directs deuterons into the plasma through a common bending magnet and injection duct. The bending magnet removes any charged deuterons that remain in the beams following neutralization and deflects them into the ion dump. The calorimeter, shown in the out-of-beam position, is used to calibrate the ion sources. This is accomplished by lowering the calorimeter into the beam path.

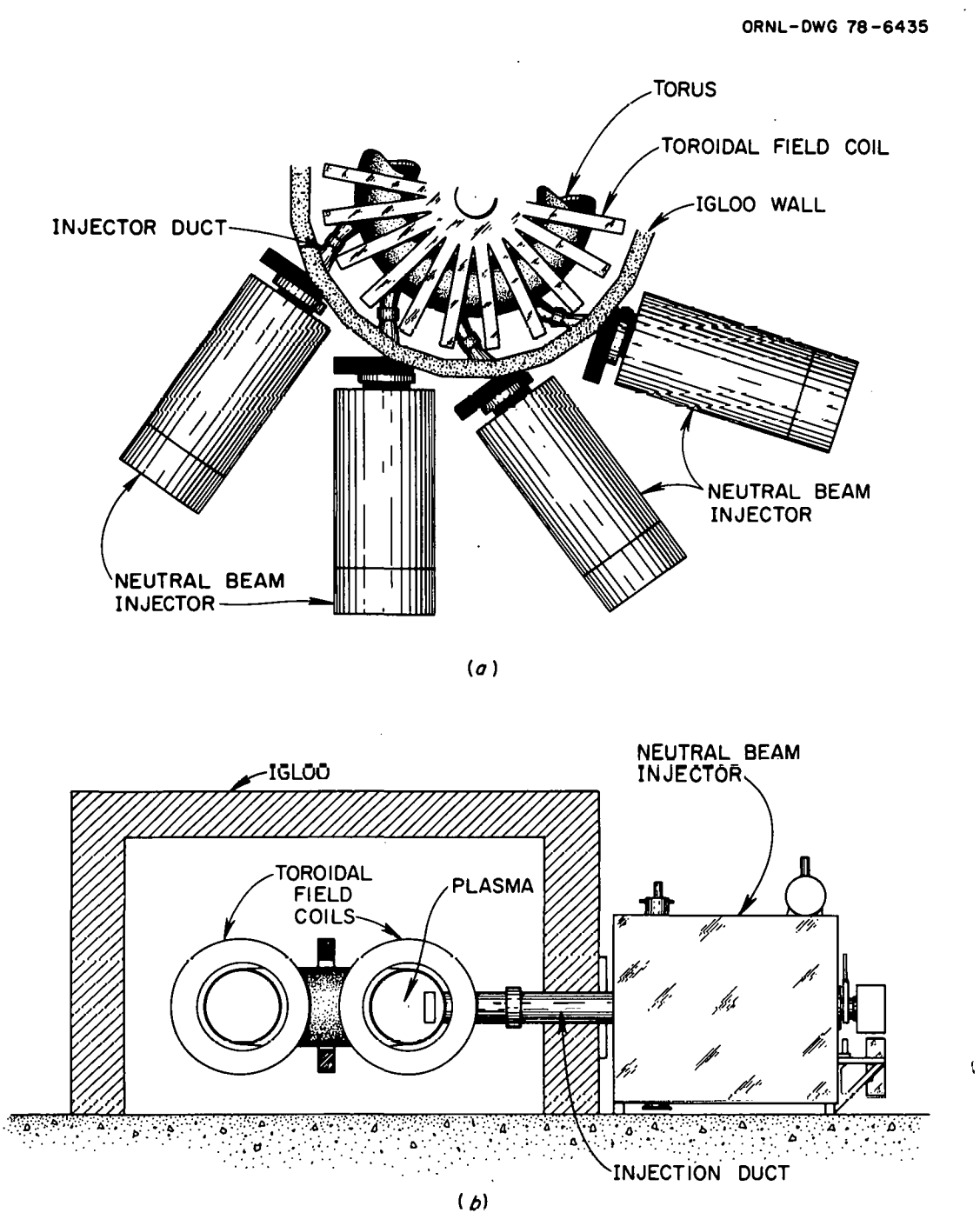

Fig. 1. Plan (a) and elevation (b) views of the neutral beam injectors and their locations relative to the igloo wall and the TFTR.

In the actual design, the shape and cross sectional area of the duct varies. For this study, the cross-sectional area was held constant and taken to be an average of the various duct sections. In the three-dimensional calculational model for the injector, the duct was taken to be rectangular in shape having a cross sectional area of 62 x 80 cm^2. In the two-dimensional model, the duct was treated as a cylinder having an inner radius of 42 cm. In both cases, the duct wall thickness is 2.54 cm and composed of SS-316.

The concrete igloo serves as the primary radiation shield between the reactor and external equipment, including the injector. The design of the TFTR does not include shielding immediately about the torus and except for the attenuation of the radiation by the toroidal field coils, the isolation of the injectors from the plasma radiation depends mainly on the igloo shield. The neutrons will, however, stream through the injection duct openings in the igloo wall and interact in the injector components. Some of the neutrons will also leak through the igloo wall. The components in the injector that are most sensitive to the neutron induced responses are the cryocondensation pumping panels, the bending magnet, and the deuteron sources. The cryopanels are designed to operate at cryogenic temperatures ($\sim$ 4°K). The nuclear heating can increase the panel temperature thereby increasing the cryogenic cooling demands for these systems. The heating of the bending magnet produces a heat source which influences the ambient temperature of the enclosure via heat radiation. The calculational models for the injectors include these components, as well as those whose presence is thought to have a significant affect on the neutron and gamma-ray flux, e.g., the calorimeter, ion dump, baffles, etc.

The calculational model of the neutral beam injector used in the three-dimensional analyses is shown in Fig. 2a. The model was constructed using the Combinatorial Geometry Module developed for use with the MORSE code[2] that allows for the description of any complex geometry by considering unions, intersections, and differences of simple bodies such as boxes, spheres, cylinders, etc. The dimensions and compositions of the injector components were taken from engineering drawings[7].

The cryocondensation pumping panels, bending magnet, calorimeter, neutralizing tubes, and baffles were represented in reasonable detail. The ion dump was approximated as a slab in a plane parallel to the exit face of the bending magnet. Only the central ion source assembly was included in the model since it was assumed that the nuclear responses in the adjacent sources would not be significantly different. The concrete floor was included in the model to account for the radiation scattered into the injector by the floor. The injection duct and igloo wall were also modelled.

In the two-dimensional calculations, the injector was represented using r-z geometry with symmetry about the z-axis as shown in Fig. 2b. The injector housing and the components were approximated using 41 radial and 120 axial mesh intervals. The vacuum enclosure was taken to be a right circular cylinder having an inner radius of 132 cm, a wall thickness of 2 cm, and a length of 570 cm. A concentric cylinder having an inner radius of 122 cm and a thickness of 1 cm was used to describe the cryopanels. In this model, the cryopanels are treated as a single layer of material rather than as separate components as in the three-dimensional model. The bending magnet was approximated by a right-circular cylinder.

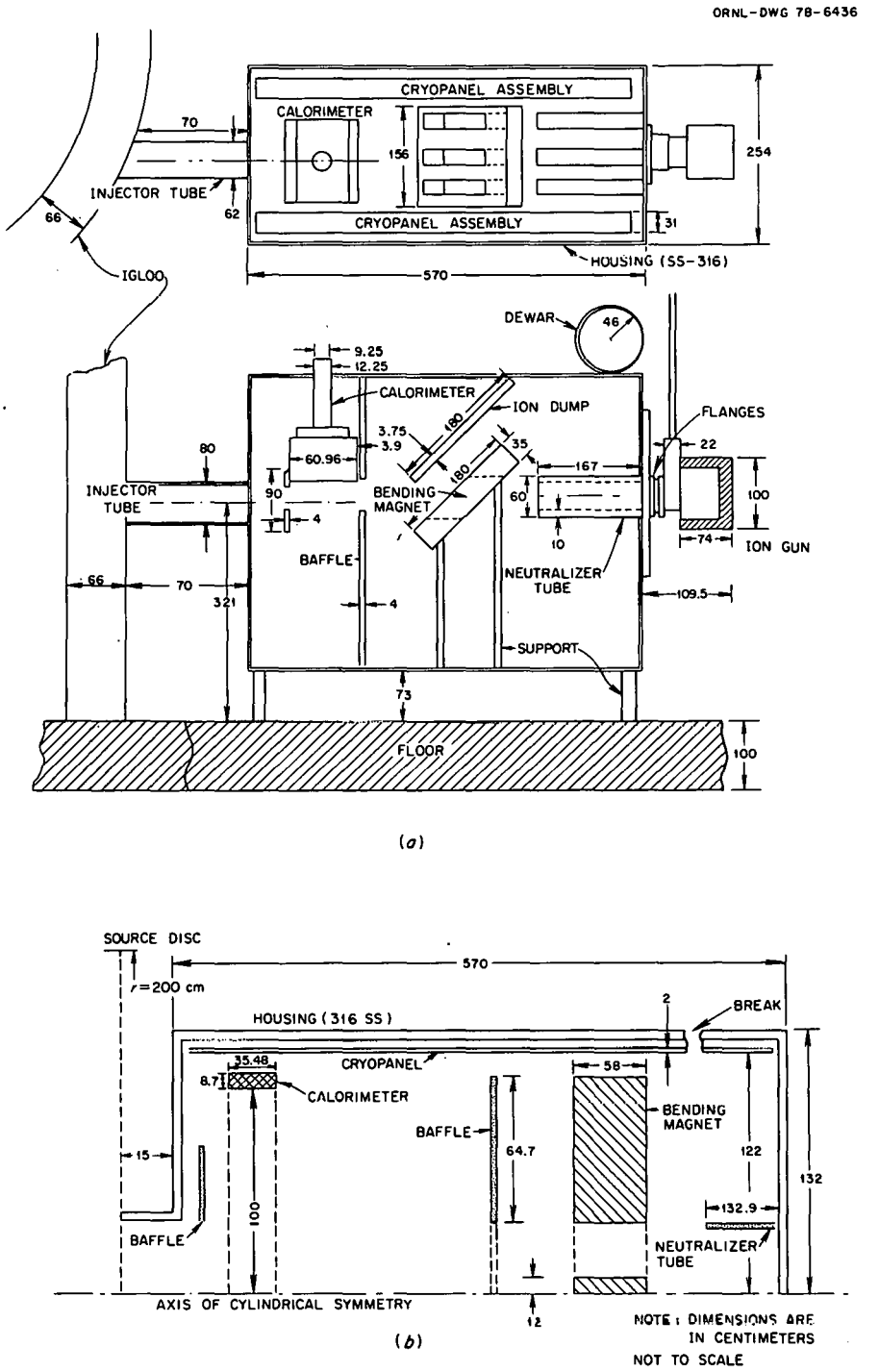

Fig. 2. Three-Dimensional (a) and two-dimensional (b) calculational models of the neutral beam injector and its various components.

The orientation of the magnet relative to the beam axis cannot be accounted for in this geometry. The dimensions of the magnet were determined by maintaining the height of the magnet and conserving total weight. The dimensions of the calorimeter were obtained in the same manner. The neutralizer tube was represented as a cylindrical tube. The igloo wall is not included in the two-dimensional model. The line labelled "Source Disc" is the surface from which the neutrons and gamma rays incident on the injector emanate. The procedure for locating the source at this position and for obtaining the contributions to the radiation from the duct and igloo wall position is discussed below.

The TFTR dimensions and materials and the parameters of the neutral beam injectors are summarized in Table 1. The compositions and nuclear densities of the various materials used in the calculations are given in Table 2.

B. Details of the Calculations

The calculational sequences used in performing the two- and three-dimensional radiation transport analyses are shown in Fig. 3. The procedures used to obtain the radiation source term for each of the injector analysis calculations are described at the top of the figure. The calculational sequences for carrying out the radiation transport in the neutral beam injector are described in the lower portion of the figure.

In the source preparation, the energy, spatial, and angular distributions of the neutrons and secondary gamma rays that stream through the injector duct and leak through the igloo wall were obtained. An initial calculation was performed using the DOT code[3] to define an interior boundary source term in the igloo using the TFTR and igloo calculational

Table 1. TFTR and Neutral Beam Injector Details

Plasma Region		
Major radius (cm)		248
Minor radius[+] (cm)		111
Instantaneous source strength (n/sec)		7×10^{18}
Reactor Components		
	Plasma Liner	Toroidal Field Coils
Composition	SS-316	copper*
Minor radius (cm)	114	140
Thickness (cm)	1	54
Major radius (cm)	265	280
*5-cm-thick SS-316 structural members on the inner and outer radial surfaces		
Concrete Igloo Shield		
Composition		Borated concrete
Wall and roof thickness (cm)		66
Dimensions from plasma center to		
wall (cm)		510
roof (cm)		260
Neutral Beam Injector		
Pulse duration (sec)		0.5
Duty factor		1.67×10^{-3}
Deuteron energy (keV)		120
Pulse repetition rate (hr^{-1})		12

[+]Plasma liner

Table 2. Composition and Nuclear Densities of Materials

Material	Composition	Nuclear Density (atoms/cm^3)
SS-316	Fe	5.43×10^{-2}
	Ni	1.06×10^{-2}
	Cr	1.15×10^{-2}
	Mn	1.65×10^{-3}
	Mo	1.29×10^{-3}
Igloo Concrete	H	1.53×10^{-2}
	^{10}B	2.20×10^{-4}
	^{11}B	8.90×10^{-4}
	C	1.02×10^{-2}
	O	4.27×10^{-2}
	Na	8.13×10^{-5}
	Mg	2.32×10^{-4}
	Al	1.22×10^{-4}
	Si	1.19×10^{-3}
	K	1.78×10^{-5}
	S	8.36×10^{-5}
	Ca	1.26×10^{-2}
	Fe	1.86×10^{-4}
Copper	Cu	8.48×10^{-2}
Aluminum	Al	6.02×10^{-2}
Zeolite[a]	Ca	1.80×10^{-3}
	Na	1.20×10^{-3}
	Al	4.90×10^{-3}
	Si	4.90×10^{-3}
	O	1.95×10^{-2}
Iron	Fe	8.46×10^{-2}

[a]Zeolite is a physical absorbant used in cryogenic systems to collect hydrogen and helium isotopes.

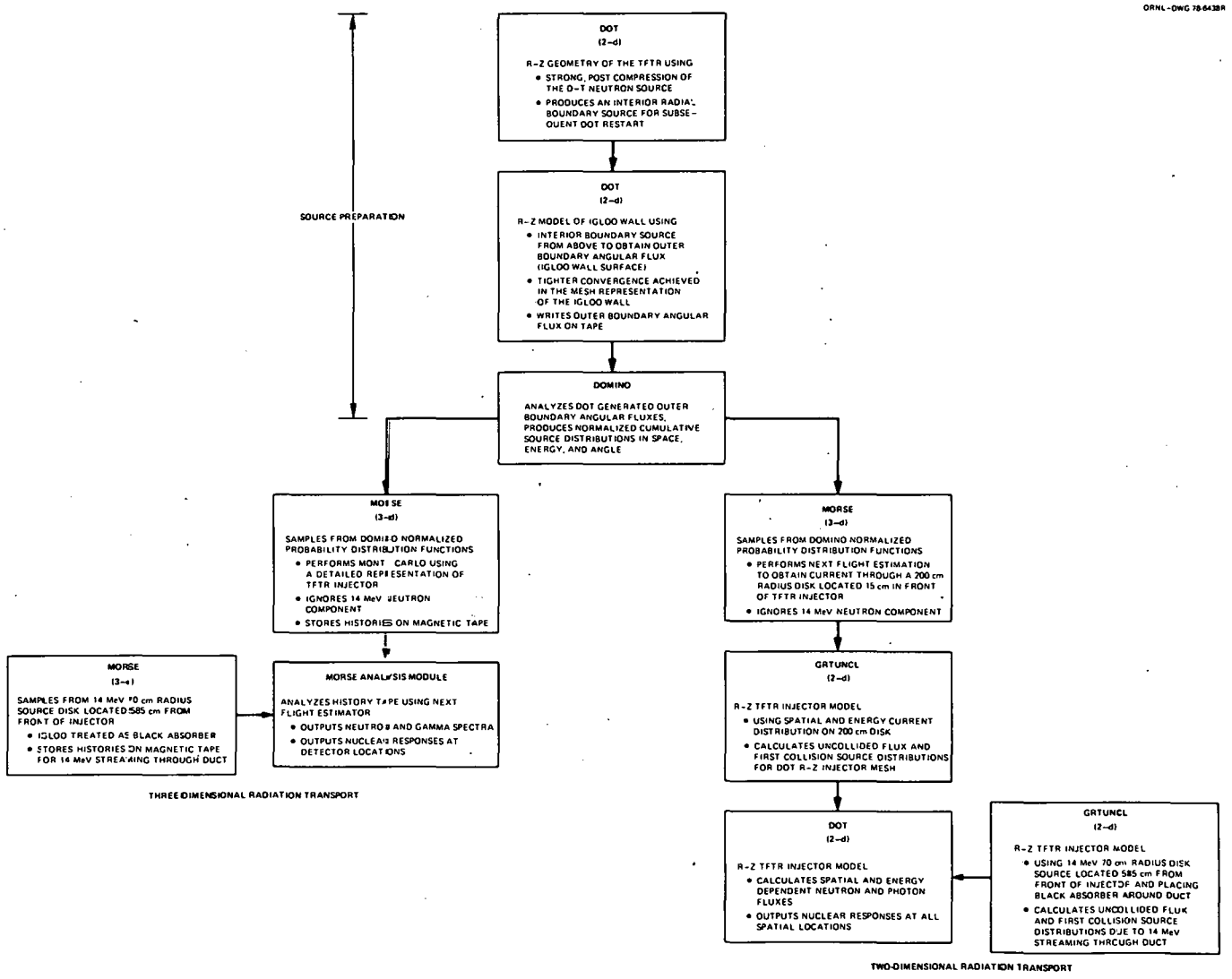

Fig. 3. Calculational sequences used to estimate the nuclear responses in the neutral beam injector.

model shown in Fig. 4. The reactor and the igloo were represented in r-z geometry with toroidal symmetry about the z-axis. The components were modelled using 61 radial and 38 axial mesh intervals. The toroidal symmetry of the system and the toroidal shape and distribution of the D-T neutron source in the plasma region are accounted for in this geometry. The neutron distribution in the plasma, shown in the inset in Fig. 4, was taken to be that at strong post-compression, the condition at which it is anticipated that the neutron yield will be the greatest[8]. The toroidal field coils were not included in the calculational model. It is not possible to account for the toroidal extent of the coils in a two-dimensional geometry, so the calculation was made with the coils excluded. Omitting the coils leads to an overestimate of the neutron and gamma-ray flux at the outer boundary of the igloo, so the nuclear responses in the neutral beam injector may be conservative.

The interior boundary source distribution obtained in this calculation includes the neutrons emitted directly from the plasma as well as those scattered by the reactor yoke, poloidal trim coils, and from the igloo concrete. The gamma rays produced by the neutron reactions in these components are also accounted for in the source term.

The interior boundary source was then used as the input to a second DOT calculation to obtain the angular flux at the radial boundary of the igloo. In these calculations, the igloo was represented in r-z geometry using 26 radial and 38 axial mesh intervals. The symmetry was maintained about the axis of toroidal symmetry of the TFTR. The motivation for calculating the boundary angular flux separately was to obtain a tighter convergence of the flux in the finer mesh representation of the igloo in

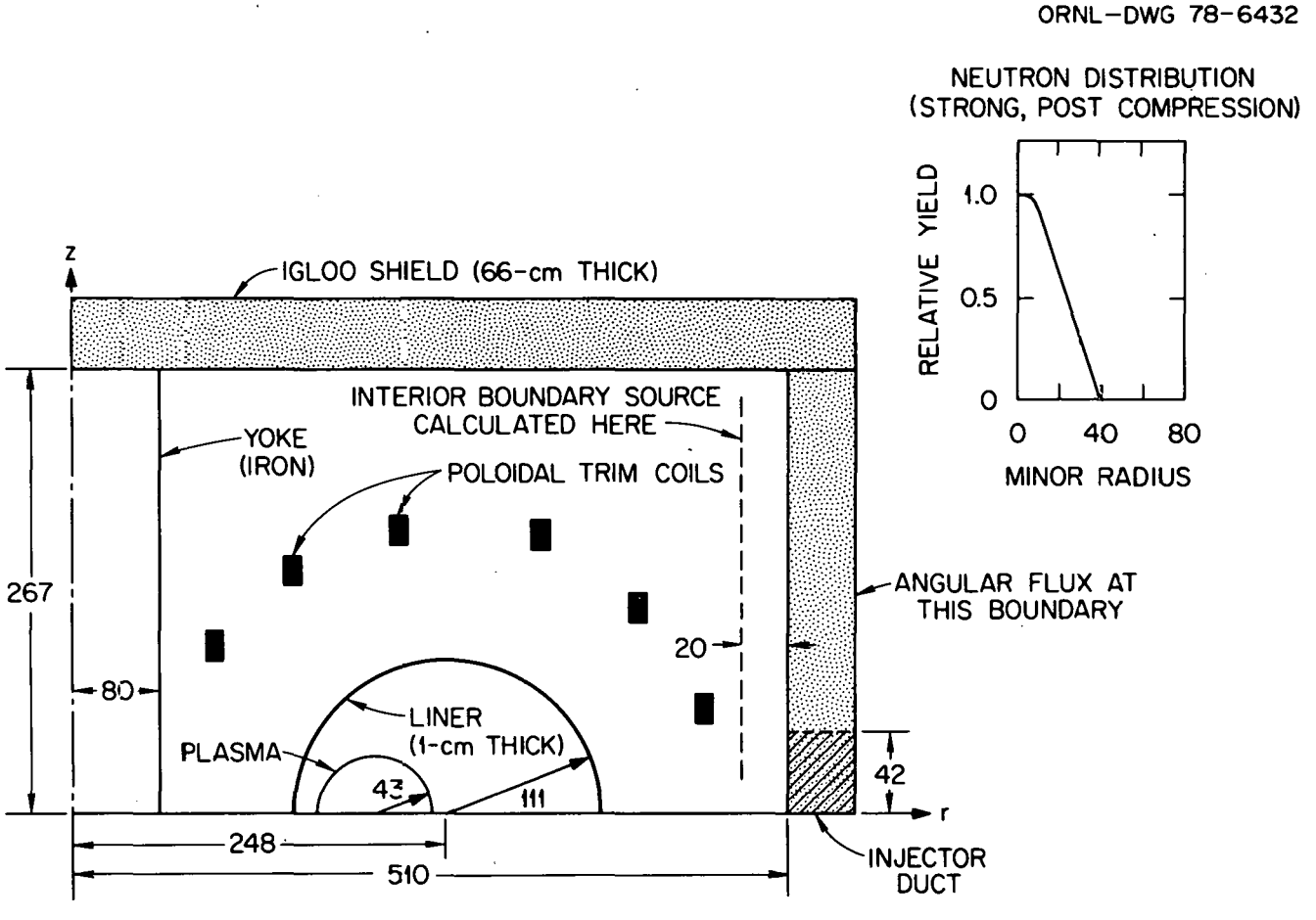

Fig. 4. Two-dimensional calculational model of the TFTR and the igloc used to obtain the energy, spatial, and angular distributions of neutrons and gamma rays incident on the injector.

the reduced geometry. Two separate calculations were performed in the reduced geometry to obtain the boundary flux "with" and "without" the injector duct in the igloo wall. For the case "with" the injector duct, the shaded portion of the igloo wall shown in Fig. 4 was treated as a void. In a two-dimensional geometry, the duct opening extends completely about the torus. The finite toroidal extent of the duct opening was accounted for in the MORSE code[2] for the three-dimensional analysis and in the preparation of the disc source used as the input to the two-dimensional analysis as described below.

The boundary angular flux data for the cases "with" and "without" the injector penetration were then each processed using the DOT-to-MORSE coupling code DOMINO.[9] This code produces cummulative distributions in energy, space and polar and azimuthal angles for subsequent source input to the MORSE code.[2] The boundary flux data for the case "with" the injector penetration was processed for all but the 14-MeV neutron group. This represents the 14-MeV neutrons which stream through the injector duct opening in the igloo. These neutrons are not properly accounted for in the DOT boundary angular flux data because the S_8 quadrature used in the DOT toroidal calculations does not contain angular directions that permit streaming along the radial axis. While this can be remedied using a highly biased and consequently large tailored quadrature set, the computational time for the toroidal calculations would be prohibitively long. All energy groups were processed for the case "without" the injector penetration.

In the three-dimensional radiation transport the sequence of collisions obtained by sampling the DOMINO[9] cummulative distributions was calculated using MORSE.[2] Separate random walk calculations were made using the DOMINO source data "with" and "without" the injector port. The source particles and their progeny which do not include 14 MeV neutron streaming were followed

through the detailed injector model shown in Fig. 2a and their histories were stored on magnetic tape. For the case "without" the duct, particles were sampled from the entire igloo surface viewed by all portions of the injector. However, those particles which would have been emitted from the area of the igloo surface corresponding to the duct opening were rejected. The random walk calculations for both the "with" and "without" cases were carried out for 5000 source particles.

The 14 MeV neutrons streaming through the injector port which were not included in the DOMINO source data were accounted for in a separate Monte Carlo calculation. In this calculation, a 70 cm radius isotropic 14 MeV neutron source disk was placed at the intersection of the axis of injection and the plasma toroidal axis. This location which corresponds to a distance of 585 cm from the front of the injector housing was chosen such that the disk source represented the plasma volume viewed through the duct opening by the injector. To ensure that neutrons emitted from this source passed only through the duct opening, the remaining portion of the igloo was treated as a black absorber. The sequence of collisions obtained by sampling the disk source was again calculated with MORSE using 5000 source particles in the random walk calculations. The number of collisions was properly normalized to account for the viewed plasma volume and the resulting normalized data was stored on magnetic tape.

The collision history tapes written by MORSE were analyzed in a separate module to determine the neutron and gamma-ray scalar flux at seven locations in the injector as shown in Fig. 5. Point detector estimators were used to obtain these data. The point estimation technique[2] scores, at each collision point, the probability that the next event will be at the detector. The next-event estimator takes into account both the

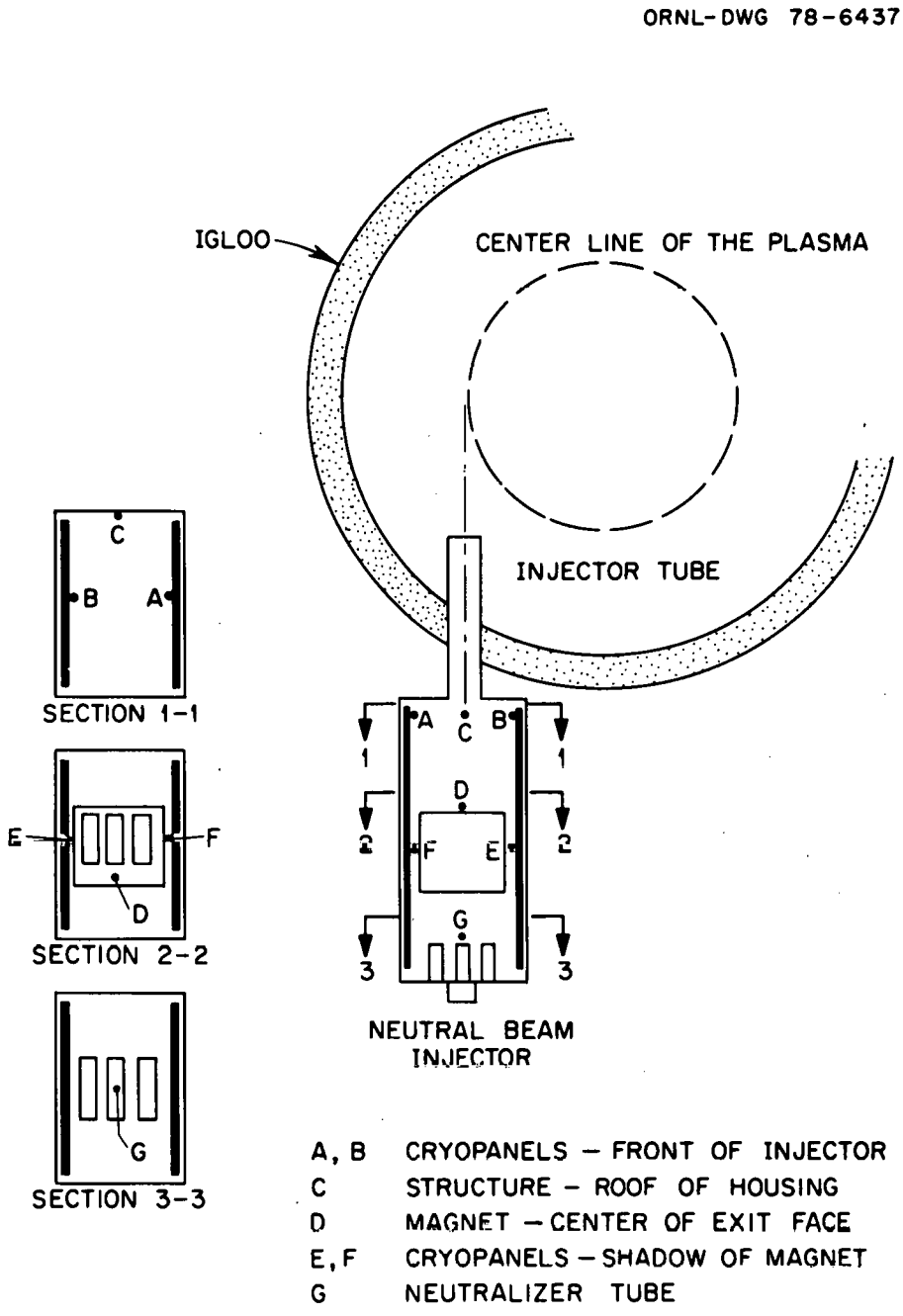

Fig. 5. Locations of the detectors in the three-dimensional calculational model relative to the injection duct and igloo wall.

uncollided and collided flux. The neutron and gamma ray spectra were estimated at each detector site and the energy integrated neutron and gamma-ray heating rates, $H_i(\bar{r})$, at the detector locations were obtained by evaluating the expression

$$H_i(\bar{r}) = \int_{\substack{\text{all particle} \\ \text{energies}}} \phi_i(\bar{r},E)\, R_i(E)\, dE, \qquad i = n,\gamma$$

where $\phi_i(\bar{r},E)$ is the scalar flux for a particle of type i and energy E at detector locations $\bar{r}$ and $R_i(E)$ is the flux-to-heating rate conversion factor for a particle of type i at energy E.

The radiation source for the two-dimensional analysis was obtained by calculating the radially-varying multigroup current through a 200-cm-radius disc labelled "Source Disc" in Fig. 2b, located 15 cm in front of the injector housing. The disc was divided into 20 radial and 10 azimuthal intervals centered about the axis of injection and the current was calculated using the point detector estimator in a separate MORSE[2] code. The normalized cummulative distributions from DOMINO for the configurations "with" and "without" the duct penetration that were used in the three-dimensional analysis also served as the input to the disc source preparation. The radial variation and total source strength were obtained by summing the contributions to the current over the azimuthal intervals and correcting for the anisotropy of the DOMINO source, respectively. The radiation source used to account for the 14 MeV streaming was approximated by the same 70 cm radius disk as that used in the three-dimensional analysis. The location of the disk and the treatment of the igloo wall, i.e., as a black absorber, was also the same.

The uncollided flux and first collision source in the injector for both the 200- and 70-cm radius disk sources were then obtained using GRTUNCL[10]. This code calculates the uncollided flux and the first collision source at each mesh interval in the injector geometry in Fig. 2b and records these data on magnetic tape for subsequent use in DOT[3]. The advantage of employing GRTUNCL is the elimination of ray effects. The uncollided flux and first collision source data obtained from the two GRTUNCL calculations was normalized and summed over all mesh intervals and used as the input to DOT.

The DOT code using the first collision source as input completes the radiation transport and adds the collided flux distribution to the uncollided flux from GRTUNCL. The spatial distributions of the nuclear heating rates and the neutron and gamma-ray scalar flux distributions in the injector were calculated in the DOT code.

In all of the calculational procedures, the radiation transport was performed using a 35-neutron, 21-gamma-ray energy group transport library. These data were obtained by collapsing the 100-neutron, 21-gamma-ray energy group DLC-37[ENDF/B-IV] data set[11]. In all cases, the scattering cross sections were represented with a P_3 Legendre expansion. The two-dimensional calculations were carried out using an S_8 angular quadrature. The nuclear heating rates were estimated using neutron and gamma-ray kerma factors generated by the MACK[12] and SMUG[13] codes, respectively.

III. DISCUSSION OF RESULTS

The calculated nuclear heating rates at four locations in the cryocondensation pumping panels corresponding to points A,B,E, and F in Fig. 5 are summarized in Tables 3-6, respectively. In the three-dimensional model, these points are in the same plane as the axis of injection. The neutron, gamma-ray, and total (neutron plus gamma-ray) heating rates are given in SS-316, copper, zeolite, and aluminum; materials that are commonly found in these panels. The results from the three-dimensional calculation, labelled MORSE, show the contributions to the heating rates from the radiation that streams through the injection port and from that leaking through the igloo wall. The numbers in parenthesis below these entries are the fractional standard deviations in the calculated results. The heating rates estimated using the two-dimensional analysis, labelled DOT, are due to the combination of these sources. The entries in the tables labelled MORSE/DOT ratios indicate the range of agreement among the heating rates obtained using the two analysis procedures.

The data in the tables, as well as the remainder of the data to be presented, have been normalized to 7×10^{18} n/sec. This corresponds to the number of neutrons produced in the TFTR in a single D-T pulse. It should be noted that the heating rates given in Tables 3 and 4 and in Tables 5 and 6 for the two-dimensional calculations are the same. The symmetry of the two-dimensional injector model does not allow for the proper orientation of the cryopanels relative to the injection duct and the igloo wall.

Table 3. NUCLEAR HEATING RATES IN THE CRYOPANEL AT DETECTOR LOCATION A

	Nuclear Heating Rates (Watts/cm³)											
	Type 316 Stainless Steel			Copper			Zeolite			Aluminum		
	Neutron	Gamma-Ray	Total	Neutron	Gamma-Ray	Total	Neutron	Gamma-Ray	Total	Neutron	Gamma-Ray	Total
MORSE[a]												
Injector Port	1.74×10^{-4}	9.52×10^{-4}	1.12×10^{-3}	2.54×10^{-4}	1.18×10^{-3}	1.42×10^{-3}	1.08×10^{-4}	9.28×10^{-5}	2.01×10^{-4}	1.74×10^{-4}	2.96×10^{-4}	4.71×10^{-4}
	(0.057)	(0.264)	(0.233)	(0.055)	(0.252)	(0.234)	(0.043)	(0.270)	(0.239)	(0.048)	(0.264)	(0.175)
Igloo Wall	1.24×10^{-4}	1.18×10^{-3}	1.31×10^{-3}	1.19×10^{-4}	1.42×10^{-3}	1.54×10^{-3}	5.75×10^{-5}	1.27×10^{-4}	1.85×10^{-4}	1.03×10^{-4}	4.01×10^{-4}	5.04×10^{-4}
	(0.644)	(0.459)	(0.416)	(0.589)	(0.449)	(0.415)	(0.632)	(0.457)	(0.424)	(0.610)	(0.486)	(0.400)
Total	2.98×10^{-4}	2.13×10^{-3}	2.43×10^{-3}	3.73×10^{-4}	2.60×10^{-3}	2.96×10^{-3}	1.56×10^{-4}	2.20×10^{-4}	3.86×10^{-4}	2.81×10^{-4}	6.97×10^{-4}	9.75×10^{-4}
	(0.666)	(0.530)	(0.477)	(0.592)	(0.515)	(0.502)	(0.633)	(0.531)	(0.487)	(0.612)	(0.553)	(0.437)
DOT[b]	2.09×10^{-4}	1.09×10^{-3}	1.30×10^{-3}	2.13×10^{-4}	1.34×10^{-3}	1.55×10^{-3}	1.15×10^{-4}	1.10×10^{-4}	2.25×10^{-4}	1.92×10^{-4}	3.48×10^{-4}	5.50×10^{-4}
MORSE/DOT Ratios[c]	0.5-2.4	0.9-3.0	1.0-2.8	0.7-2.8	0.9-2.8	1.0-2.9	0.5-2.4	0.9-3.1	1.0-2.6	0.6-2.4	0.9-3.1	1.0-2.5

[a] Three-Dimensional Calculation

[b] Two-Dimensional Calculation

[c] $(H(MORSE) \times (1-fsd))/H(DOT) - (H(MORSE) \times (1+fsd))/H(DOT)$

fsd = fractional standard deviation

Table 4. NUCLEAR HEATING RATES IN THE CRYOPANEL AT DETECTOR LOCATION B

	Nuclear Heating Rates (Watts/cm³)											
	Type 316 Stainless Steel			Copper			Zeolite			Aluminum		
	Neutron	Gamma-Ray	Total	Neutron	Gamma-Ray	Total	Neutron	Gamma-Ray	Total	Neutron	Gamma-Ray	Total
MORSE[a]												
Injector Port	7.80×10^{-4}	1.19×10^{-3}	1.98×10^{-3}	7.59×10^{-4}	1.50×10^{-3}	2.26×10^{-3}	3.94×10^{-4}	7.33×10^{-4}	1.13×10^{-3}	6.09×10^{-4}	6.09×10^{-4}	1.22×10^{-3}
	(0.113)	(0.144)	(0.096)	(0.092)	(0.132)	(0.095)	(0.088)	(0.175)	(0.098)	(0.097)	(0.107)	(0.097)
Igloo Wall	3.77×10^{-5}	3.55×10^{-3}	3.59×10^{-3}	5.12×10^{-5}	4.41×10^{-3}	4.91×10^{-4}	2.35×10^{-5}	3.56×10^{-5}	5.92×10^{-5}	3.72×10^{-5}	1.13×10^{-3}	1.50×10^{-4}
	(0.201)	(0.205)	(0.187)	(0.248)	(0.199)	(0.181)	(0.298)	(0.229)	(0.177)	(0.262)	(0.225)	(0.179)
Total	8.18×10^{-4}	4.74×10^{-3}	5.57×10^{-3}	8.11×10^{-4}	5.91×10^{-3}	2.75×10^{-3}	4.18×10^{-4}	7.69×10^{-4}	1.19×10^{-3}	6.46×10^{-4}	1.74×10^{-3}	1.37×10^{-3}
	(0.231)	(0.251)	(0.210)	(0.265)	(0.239)	(0.204)	(0.311)	(0.288)	(0.201)	(0.279)	(0.249)	(0.204)
DOT[b]	2.09×10^{-4}	1.09×10^{-3}	1.30×10^{-3}	2.13×10^{-4}	1.34×10^{-3}	1.55×10^{-3}	1.15×10^{-4}	1.10×10^{-4}	2.25×10^{-4}	1.15×10^{-4}	1.10×10^{-4}	2.25×10^{-4}
MORSE/DOT Ratios[c]	3.0-4.8	3.3-5.4	3.4-5.2	2.8-4.8	3.4-5.5	1.4-2.1	2.5-4.7	4.9-9.0	4.2-6.4	4.0-7.2	12-19	4.9-7.3

[a] Three-Dimensional Calculation

[b] Two-Dimensional Calculation

[c] (H(MORSE) × (1-fsd))/H(DOT) - (H(MORSE) × (1+fsd))/H(DOT)
fsd = fractional standard deviation

Table 5. NUCLEAR HEATING RATES IN THE CRYOPANEL AT DETECTOR LOCATION E

	Nuclear Heating Rates (Watts/cm³)											
	Type 316 Stainless Steel			Copper			Zeolite			Aluminum		
	Neutron	Gamma-Ray	Total	Neutron	Gamma-Ray	Total	Neutron	Gamma-Ray	Total	Neutron	Gamma-Ray	Total
MORSE[a]												
Injector Port	4.60×10^{-6} (0.207)	4.33×10^{-5} (0.298)	4.80×10^{-5} (0.272)	1.10×10^{-5} (0.119)	5.32×10^{-5} (0.288)	6.33×10^{-5} (0.243)	4.84×10^{-6} (0.197)	4.42×10^{-6} (0.323)	9.32×10^{-6} (0.189)	6.35×10^{-5} (0.181)	1.39×10^{-5} (0.148)	2.03×10^{-5} (0.229)
Igloo Wall	5.00×10^{-6} (0.679)	1.48×10^{-5} (0.266)	1.98×10^{-5} (0.242)	5.21×10^{-6} (0.500)	1.87×10^{-5} (0.252)	2.39×10^{-5} (0.215)	2.73×10^{-6} (0.437)	1.37×10^{-6} (0.301)	4.10×10^{-6} (0.312)	4.45×10^{-5} (0.587)	4.41×10^{-6} (0.300)	8.86×10^{-6} (0.294)
Total	9.60×10^{-6} (0.710)	5.81×10^{-5} (0.399)	6.78×10^{-5} (0.364)	1.53×10^{-5} (0.514)	7.19×10^{-5} (0.383)	8.72×10^{-5} (0.324)	7.56×10^{-6} (0.525)	5.80×10^{-6} (0.442)	1.33×10^{-5} (0.365)	1.08×10^{-5} (0.614)	1.83×10^{-5} (0.335)	2.92×10^{-5} (0.373)
DOT[b]	2.49×10^{-6}	1.32×10^{-5}	1.50×10^{-5}	3.60×10^{-6}	1.62×10^{-5}	1.98×10^{-5}	1.43×10^{-6}	1.29×10^{-6}	2.72×10^{-6}	2.05×10^{-6}	4.11×10^{-6}	6.18×10^{-6}
MORSE/DOT Ratios[c]	1.1-6.6	2.6-6.2	2.9-6.2	2.1-5.4	2.7-6.1	3.0-5.8	2.5-8.1	2.5-6.5	3.1-6.7	2.0-8.5	3.0-5.9	3.0-6.5

[a] Three-Dimensional Calculation

[b] Two-Dimensional Calculation

[c] (H(MORSE) × (1-fsd))/H(DOT) - (H(MORSE) × (1+fsd))/H(DOT)
fsd = fractional standard deviation

Table 6. NUCLEAR HEATING RATES IN THE CRYOPANEL AT DETECTOR LOCATION F

	Nuclear Heating Rates (Watts/cm³)											
	Type 316 Stainless Steel			Copper			Zeolite			Aluminum		
	Neutron	Gamma-Ray	Total	Neutron	Gamma-Ray	Total	Neutron	Gamma-Ray	Total	Neutron	Gamma-Ray	Total
MORSE[a]												
Injector Port	2.51×10^{-5}	9.69×10^{-5}	1.22×10^{-4}	2.66×10^{-5}	1.19×10^{-4}	1.45×10^{-4}	1.36×10^{-5}	1.59×10^{-5}	2.29×10^{-5}	2.37×10^{-5}	5.03×10^{-5}	7.40×10^{-5}
	(0.390)	(0.661)	(0.530)	(0.783)	(0.650)	(0.541)	(0.282)	(0.388)	(0.311)	(0.315)	(0.398)	(0.397)
Ig oo Wall	3.43×10^{-6}	1.97×10^{-5}	2.32×10^{-5}	4.09×10^{-6}	2.49×10^{-5}	2.90×10^{-5}	2.05×10^{-6}	1.93×10^{-6}	3.98×10^{-6}	3.34×10^{-6}	6.09×10^{-6}	9.41×10^{-6}
	(0.549)	(0.401)	(0.362)	(0.370)	(0.387)	(0.342)	(0.408)	(0.458)	(0.321)	(0.461)	(0.454)	(0.351)
Total	2.85×10^{-5}	1.17×10^{-4}	1.45×10^{-4}	3.07×10^{-5}	1.44×10^{-4}	1.74×10^{-4}	1.57×10^{-5}	1.78×10^{-5}	2.69×10^{-5}	2.70×10^{-5}	5.64×10^{-5}	8.34×10^{-5}
	(0.673)	(0.773)	(0.642)	(0.466)	(0.756)	(0.640)	(0.496)	(0.600)	(0.447)	(0.558)	(0.604)	(0.530)
DOT[b]	2.94×10^{-6}	1.32×10^{-5}	1.50×10^{-5}	3.60×10^{-6}	1.62×10^{-5}	1.98×10^{-5}	1.43×10^{-6}	1.29×10^{-6}	2.72×10^{-6}	2.05×10^{-6}	4.11×10^{-6}	6.18×10^{-6}
MORSE/DOT Ratios[c]	3.2-16	2.0-16	3.5-16	4.6-13	2.2-16	3.0-14	5.5-16	5.5-22	5.5-14	5.8-21	5.5-22	6.3-21

[a] Three-Dimersional Calculation

[b] Two-Dimensional Calculation

[c] (H(MORSE) × (1-fsd))/H(DOT) - (H(MORSE) × (1+fsd))/H(DOT)
fsd = fractional standard deviation

The calculated heating rates at all four locations and in all of the materials are small. That is, the heating rates are not expected to seriously impact the cryogenics of the panels. The heating rates at locations E and F are approximately two orders of magnitude lower than the heating rates at positions A and B because of the greater distance of these points from the plasma and because the portion of the cryopanel at these locations are partially shielded by the bending magnet. The total heating rates in SS-316 and copper are larger than those in zeolite and aluminum. SS-316 and copper absorb more gamma rays which results in the higher heating rate.

The nuclear heating rates estimated using the three-dimensional procedure are, in most cases, larger than those obtained from the two-dimensional analysis as indicated by the MORSE/DOT ratios. This is due to a number of considerations. The three-dimensional analysis incorporates the realistic neutral beam injector model and radiation source and the heating rates obtained in this analysis are representative of those which will be encountered in operation. The two-dimensional data were obtained using an approximate injector model so it is not surprising that the MORSE/DOT ratios indicate differences in the heating rates for the two procedures. The representation of the bending magnet in the two-dimensional model combined with the inability of this model to account for the curvature of the igloo wall can lead to part of the differences in the results, particularly at detector location F.

The heating rates in SS-316, copper, zeolite, and aluminum as a function of distance in the cryopanels in the two-dimensional injector

model obtained using DOT are shown in Figs. 6 and 7. In the figures, the upper curves show the total heating rate and the lower curves show the heating rate due to neutrons only. The points with error bars are the total heating rates calculated at detector locations A and E using the MORSE code. The valley in the curves in the interval from $\sim$ 70 to $\sim$ 130 cm is due by the shielding of the cryopanels by the calorimeter. The heating rates decrease at distances beyond $\sim$ 270 cm because of the shielding by the bending magnet. The flat behavior of the curves at the distances beyond $\sim$ 350 cm is due to the radiation streaming directly from the injector duct passing through the opening in the magnet.

The heating rates at locations C, D, and G in the neutral beam injector, shown in Fig. 5, are summarized in Tables 7-9, respectively. The entries in the tables have the same meaning as those described above for Tables 3-6. Detector location C is in the "roof" of the injector housing, D is at the exit face of the bending magnet, and G is at the exit of the central neutralizer tube. The heating rates obtained using both calculational procedures are in good agreement at location C. The heating rates at locations D and G are dominated by the radiation leaking through the injector port. The data obtained using both calculational procedures are in good agreement, particularly in view of the differences in the representation of the magnet and the neutralizer tube in the two models.

The neutron and gamma-ray flux per unit energy as a function of energy at the seven locations shown in Fig. 5 calculated using the two- and three-dimensional procedures are compared in Figs. 8-14. In these figures, the solid curves show the spectra obtained from the three-dimensional analysis (MORSE) and the dashed curves show the distributions obtained from the two-dimensional calculation (DOT).

Table 7. NUCLEAR HEATING RATES IN THE INJECTOR STRUCTURE AT DETECTOR LOCATION C

(Type 316 Stainless Steel)

Method of Calculation	Nuclear Heating Rates (Watts/cm^3)		
Three-Dimensional (MORSE)	Neutron	Gamma-Ray	Total
Injector Port	2.12×10^{-4} (0.049)	6.20×10^{-4} (0.123)	8.32×10^{-4} (0.086)
Igloo Wall	1.00×10^{-4} (0.483)	4.01×10^{-4} (0.393)	5.01×10^{-4} (0.339)
Total	3.12×10^{-4} (0.485)	1.02×10^{-3} (0.412)	1.33×10^{-3} (0.350)
Two-Dimensional (DOT)	2.21×10^{-4}	1.02×10^{-3}	1.24×10^{-3}
MORSE/DOT Ratios[a]	0.7-2.1	0.6-1.4	0.7-1.4

[a] (H(MORSE) × (1-fsd))/H(DOT) - (H(MORSE) × (1+fsd))/H(DOT)
fsd = fractional standard deviation

Table 8. NUCLEAR HEATING RATES AT THE FRONT OF THE BENDING MAGNET AT DETECTOR LOCATION D

(Iron)

Method of Calculation	Nuclear Heating Rates (Watts/cm^3)		
Three-Dimensional (MORSE)	Neutron	Gamma-Ray	Total
Injector Port	8.28×10^{-4} (0.224)	7.13×10^{-4} (0.066)	1.54×10^{-3} (0.065)
Igloo Wall	1.18×10^{-5} (0.254)	8.40×10^{-5} (0.500)	9.58×10^{-5} (0.480)
Total	8.39×10^{-4} (0.291)	7.97×10^{-4} (0.504)	1.64×10^{-3} (0.484)
Two-Dimensional (DOT)	7.14×10^{-4}	8.62×10^{-4}	1.57×10^{-3}
MORSE/DOT Ratios[a]	0.83-1.51	0.46-1.40	0.54-1.55

[a] (H(MORSE) × (1-fsd))/H(DOT) - (H(MORSE) × (1+fsd))/H(DOT)
fsd = fractional standard deviation

Table 9. NUCLEAR HEATING RATES IN THE INJECTOR GUN AT DETECTOR LOCATION G

(Type 316 Stainless Steel)

Method of Calculation	Nuclear Heating Rates (Watts/cm^3)		
Three-Dimensional (MORSE)	Neutron	Gamma-Ray	Total
Injector Port	4.05×10^{-4} (0.092)	5.42×10^{-5} (0.103)	4.49×10^{-4} (0.077)
Igloo Wall	1.81×10^{-6} (0.149)	1.89×10^{-5} (0.197)	2.07×10^{-5} (0.180)
Total	4.07×10^{-4} (0.175)	7.31×10^{-5} (0.222)	6.66×10^{-4} (0.196)
Two-Dimensional (DOT)	5.94×10^{-4}	3.10×10^{-4}	9.04×10^{-4}
MORSE/DOT Ratios[c]	0.57-0.81	0.18-0.29	0.60-0.74

[d] (H(MORSE) × (1-fsd))/H(DOT) - (H(MORSE) × (1+fsd))/H(DOT)
fsd = fractional standard deviation

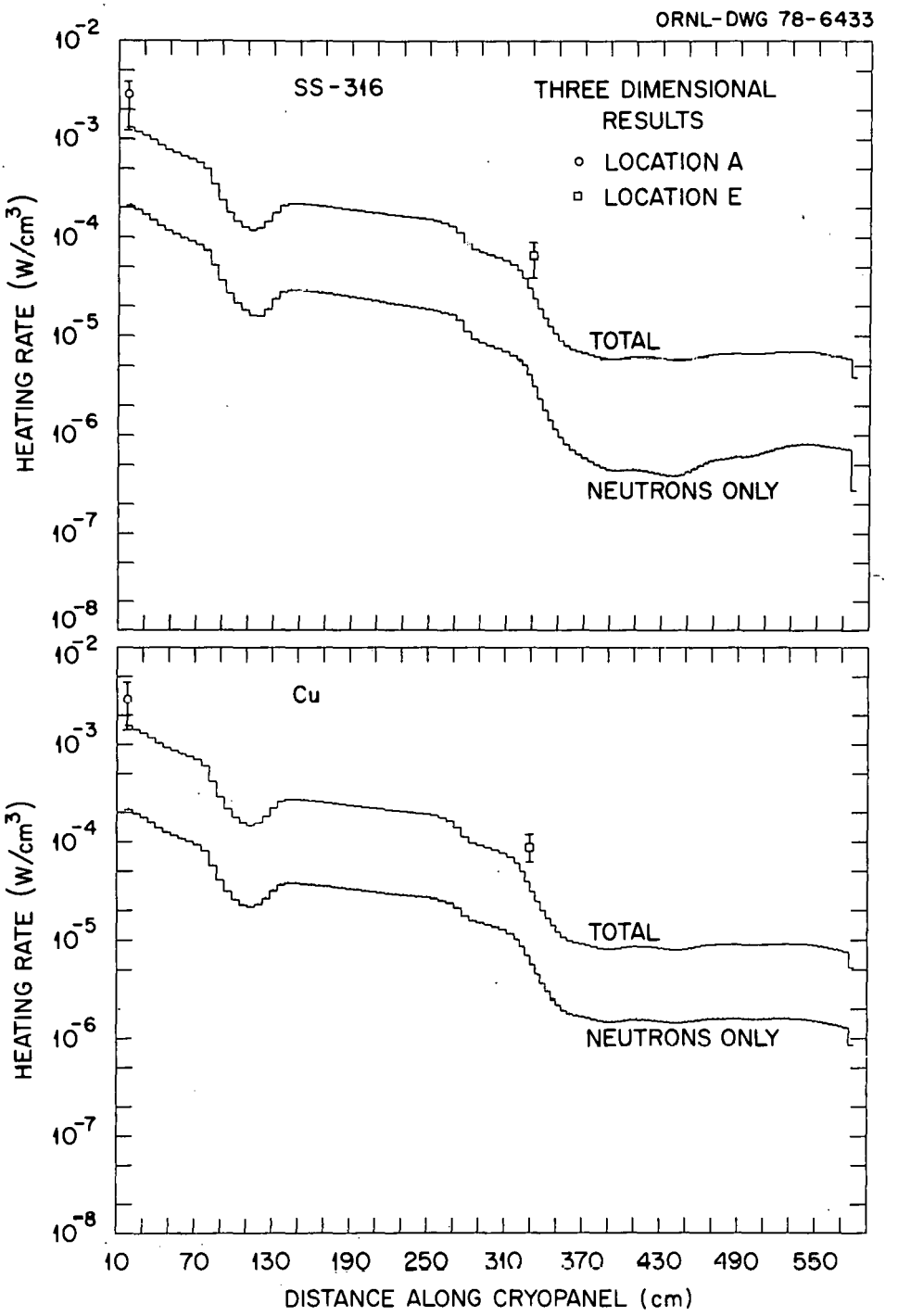

Fig. 6. Nuclear heating rates in SS-316 (a) and copper (b) as a function of distance along the cryopanel. The total heating rates at points A and E obtained from the three-dimensional analysis are also shown.

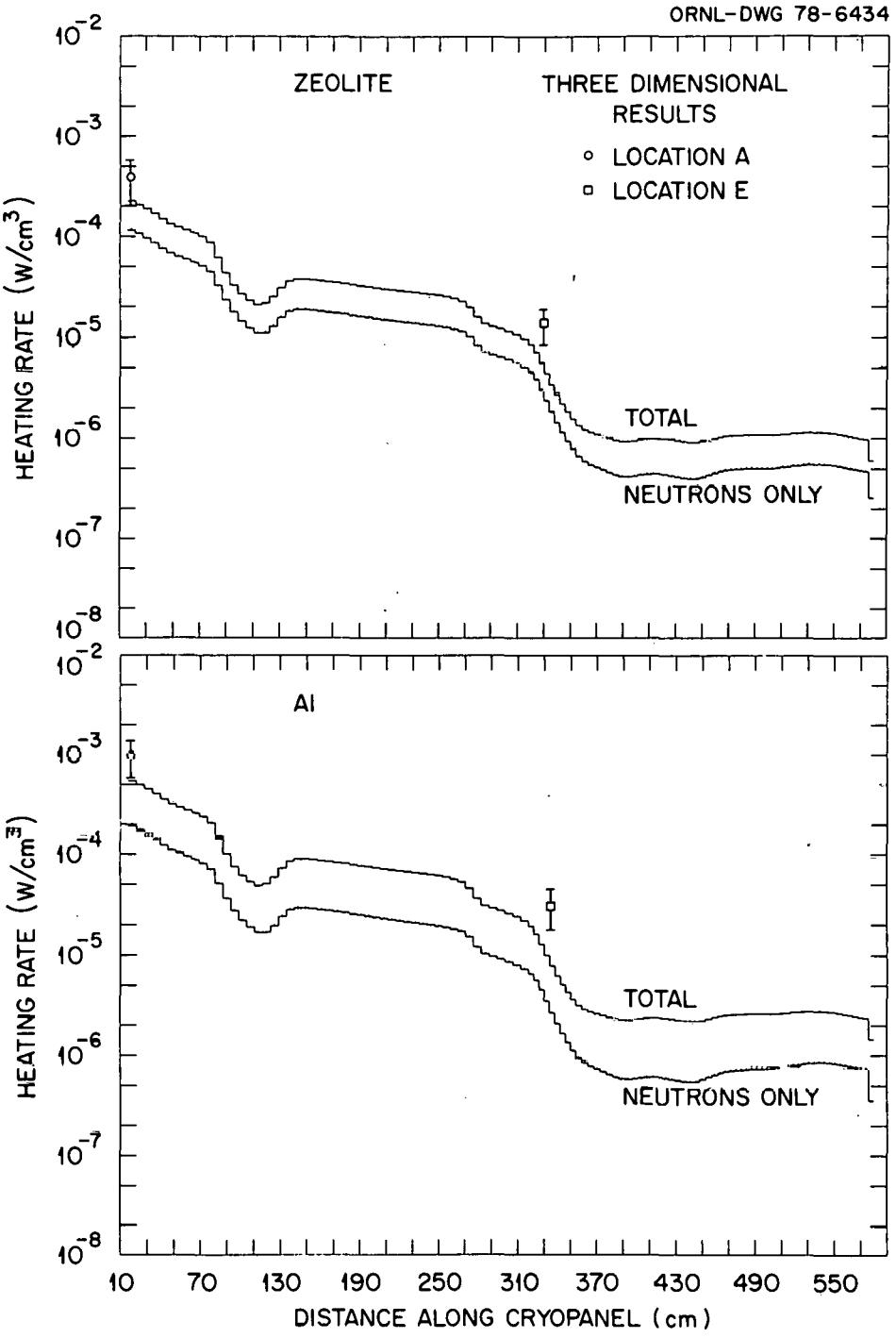

Fig. 7. Nuclear heating rates in zeolite (a) and aluminum (b) as a function of distance along the cryopanel. The total heating rates at points A and E obtained from the three-dimensional analysis are also shown.

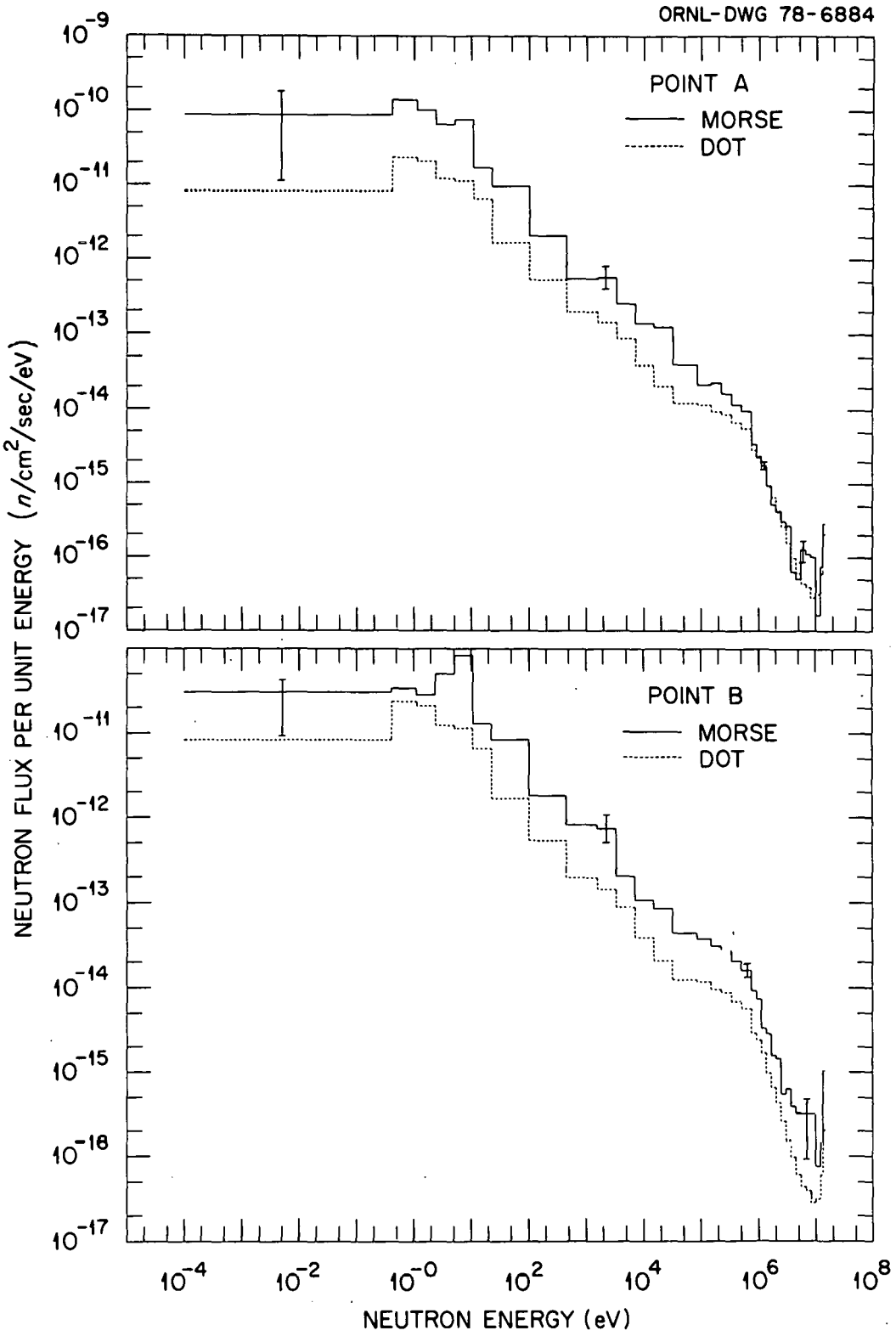

Fig. 8. Comparison of the neutron flux per unit energy at detector locations A (a) and B (b).

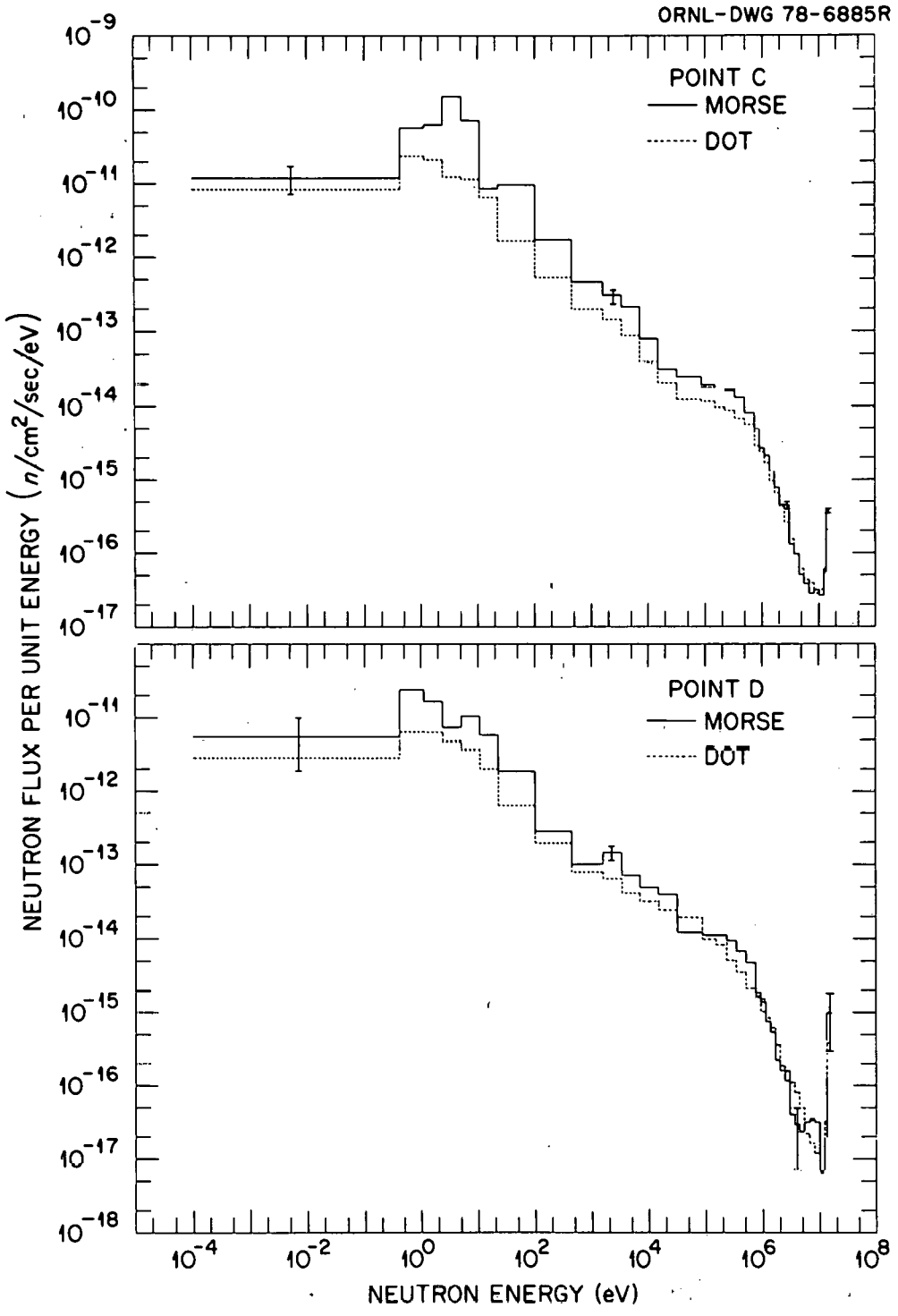

Fig. 9. Comparison of the neutron flux per unit energy at detector locations C (a) and D (b).

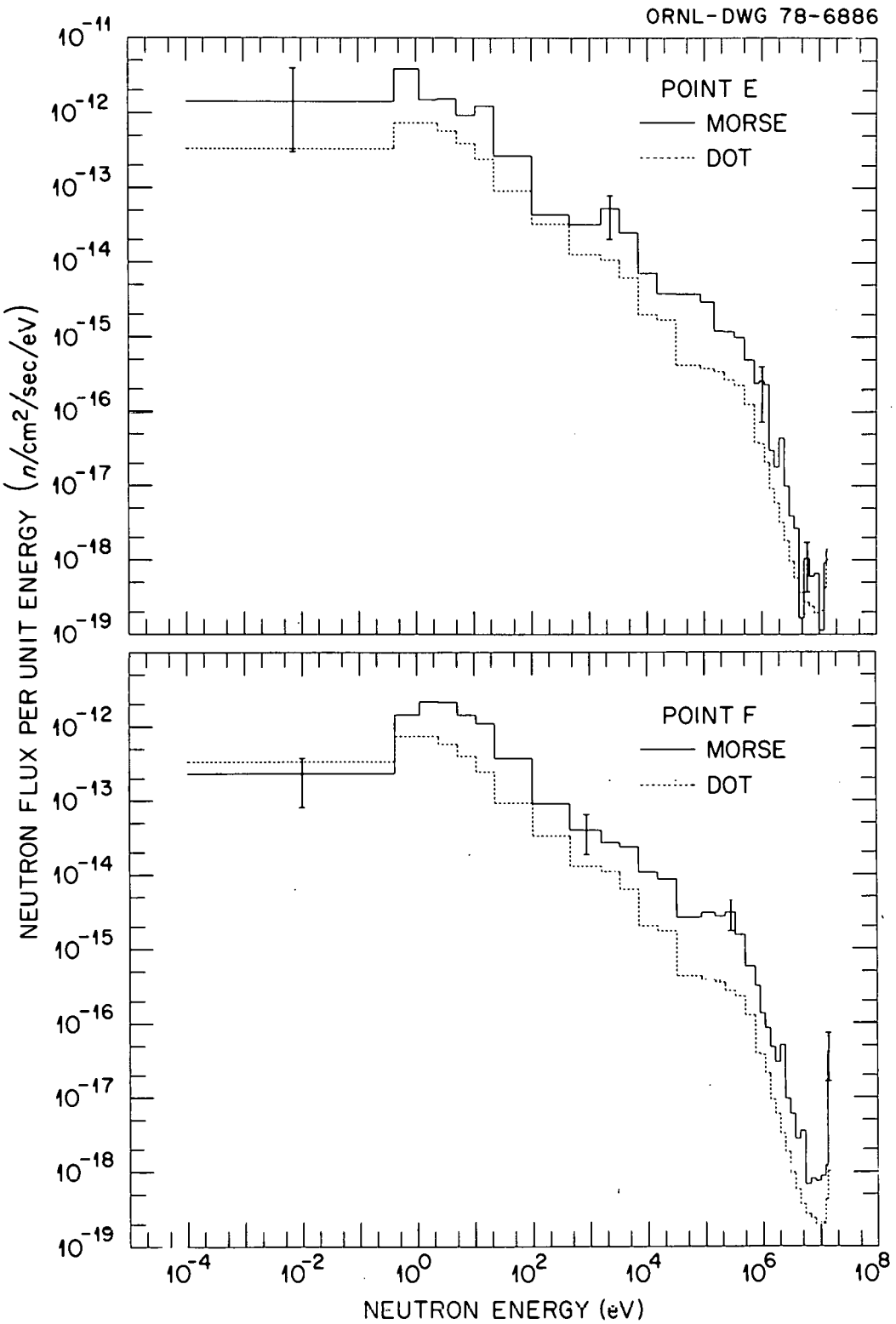

Fig. 10. Comparison of the neutron flux per unit energy at detector locations F (a) and F (b).

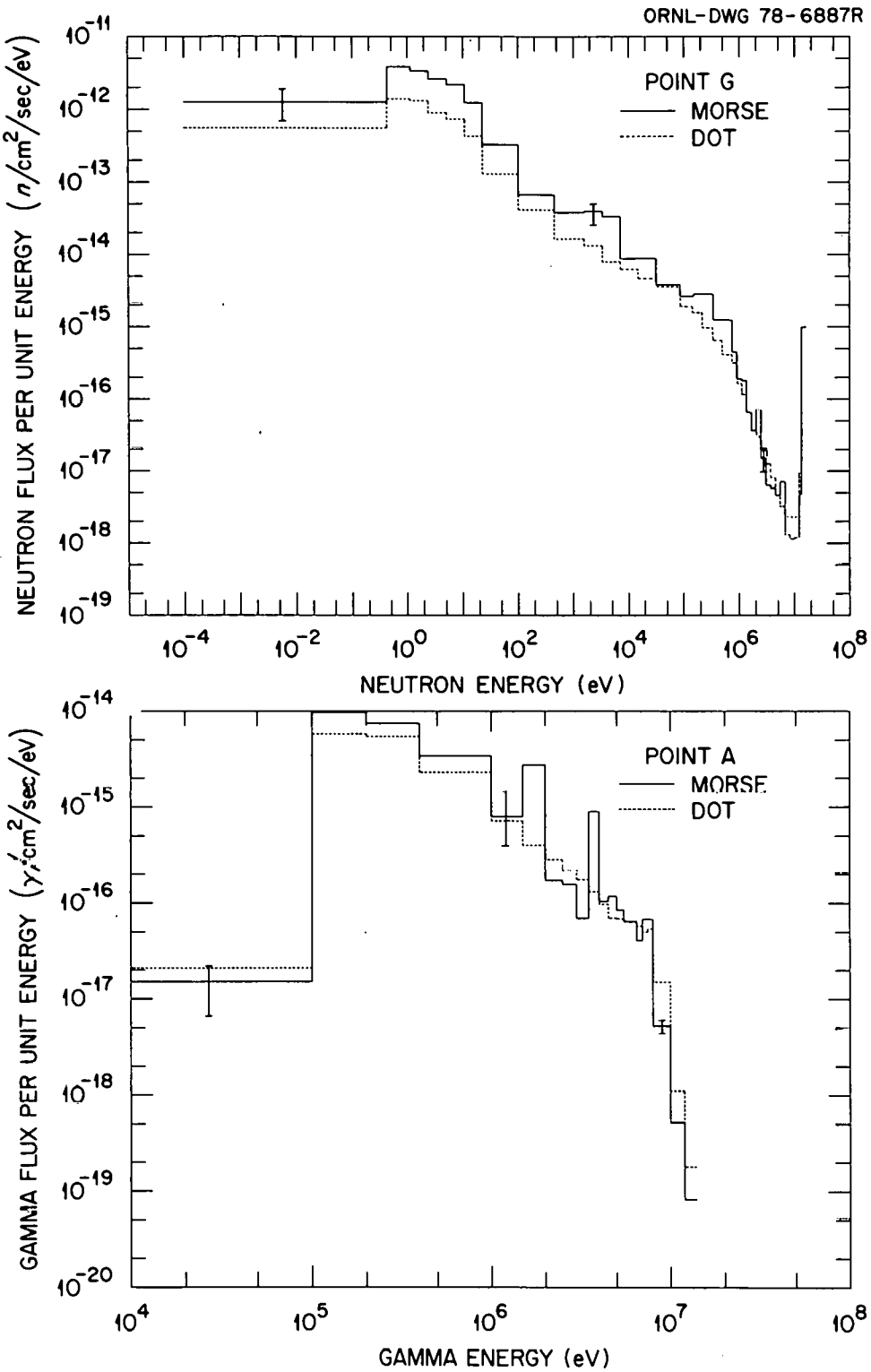

Fig. 11. Comparison of the neutron flux per unit energy at location G (a) and the gamma ray flux per unit energy at location A (b).

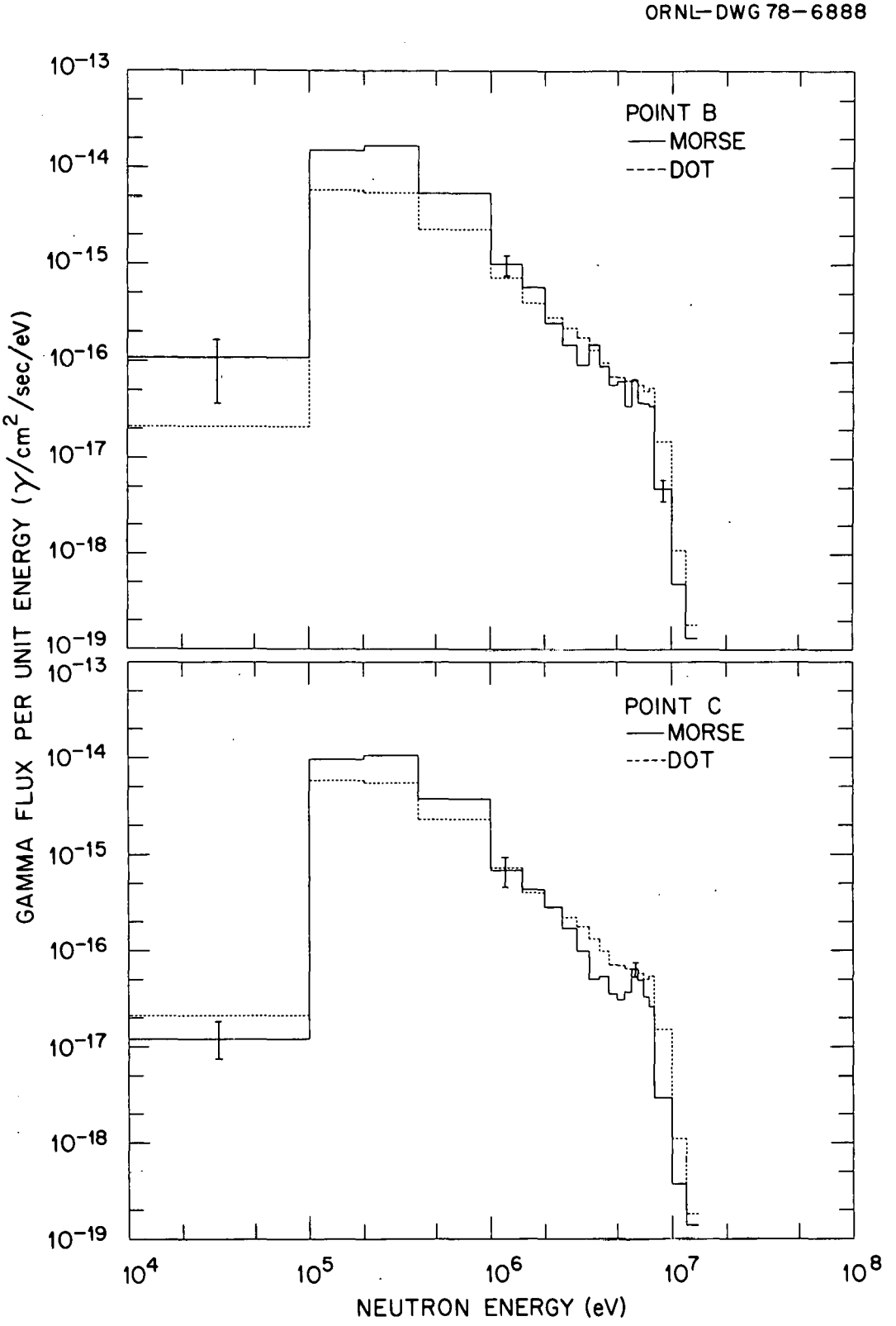

Fig. 12. Comparison of the gamma-ray flux per unit energy at locations B (a) and C (b).

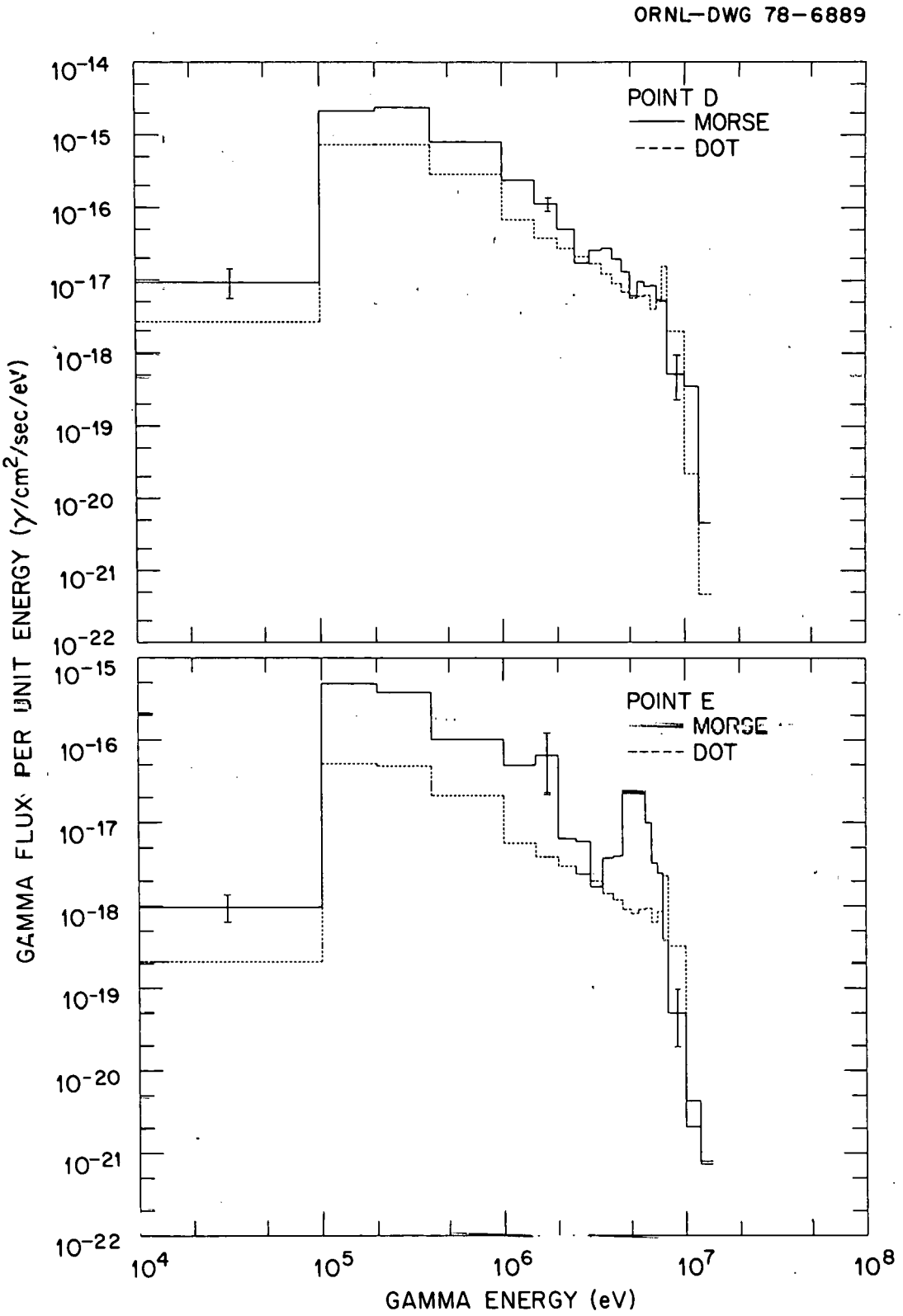

Fig. 13. Comparison of the gamma-ray flux per unit energy at locations D (a) and E (b).

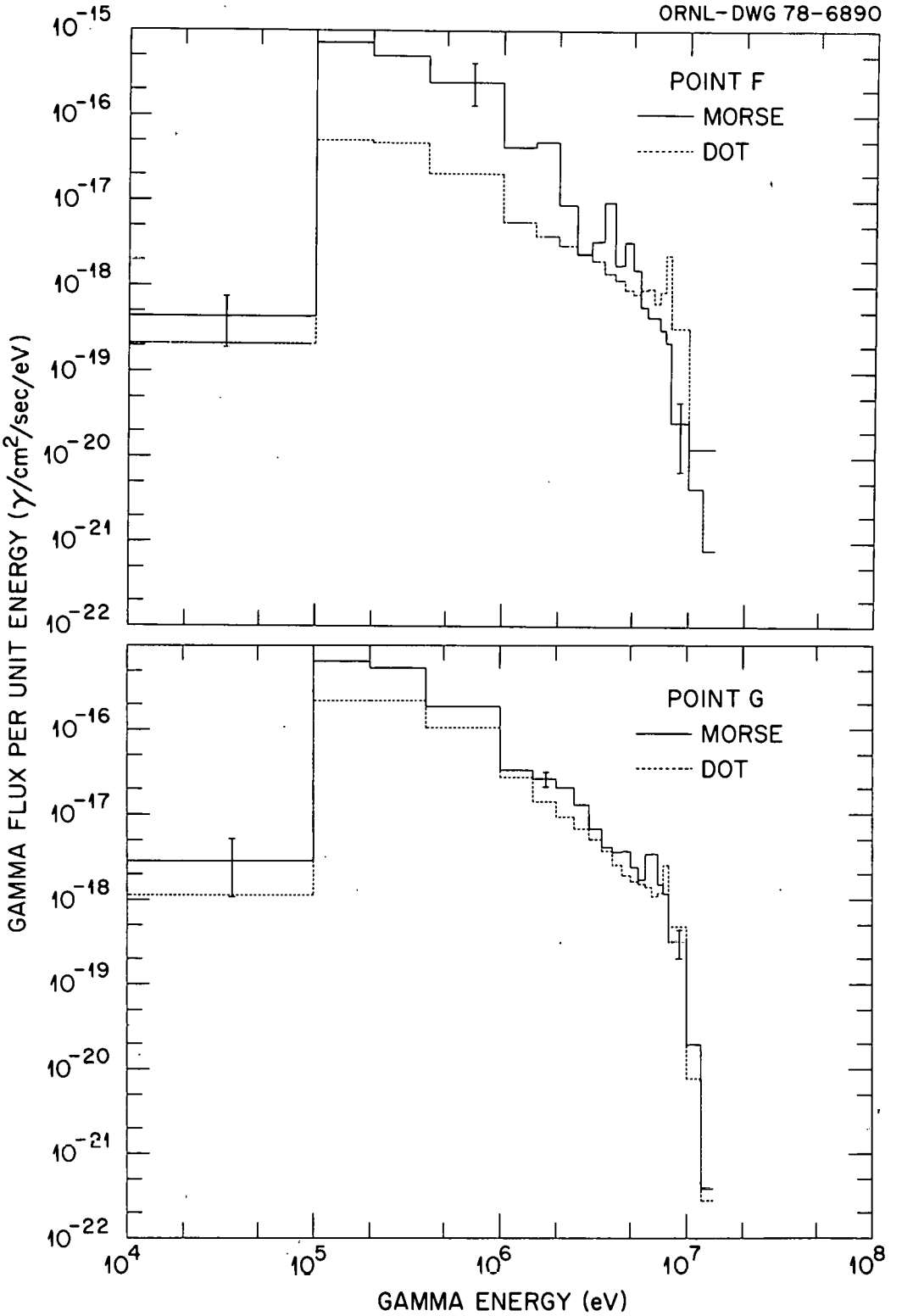

Fig. 14. Comparison of the gamma-ray flux per unit energy at locations F (a) and G (b).

The neutron spectra obtained using DOT have essentially the same energy dependence as those obtained using MORSE. At locations A, C, and G, the distributions are essentially the same at neutron energies above $\sim$ 500 keV. At lower neutron energies, the DOT calculation underestimates the flux per unit energy compared to the MORSE data with differences ranging as high as a factor of 10 in some energy intervals. At the remaining locations, the magnitude of the neutron spectra estimated using the DOT code is less than that obtained from the MORSE calculation, but the shapes of the spectra are very similar. Differences in the magnitude are as high as a factor of 10 in certain energy intervals at some of the detector locations.

The gamma-ray spectra at locations A, B, C, D, and G calculated using both radiation transport methods are, on the average, in good agreement at all energies. At gamma-ray energies below $\sim$ 5 MeV the spectra at locations E and F obtained using the two-dimensional analysis are smaller in magnitude than the spectra obtained using MORSE.

The differences in the neutron and gamma-ray spectra at the various detector locations may be attributed to the modelling of the neutral beam injector. Also, the MORSE results have statistical uncertainties that vary from $\sim$ 20% at high neutron energies (> 500 keV) to $\sim$ 60% at neutron energies (< 500 keV) in certain energy intervals.

SUMMARY

The nuclear heating rates calculated at the various detector locations in the TFTR neutral beam injector are small and not expected to impact the design or operation of these systems. The small values for the

heating rates are due to the low neutron yield of the TFTR and these responses can be scaled directly with the neutron production. When these data are extrapolated to the much higher neutron yields that may be anticipated in more advanced fusion reactor systems, particularly power reactors, serious nuclear heating problems in injector components can be expected.

The two-dimensional calculational procedure estimates the heating rates and neutron and gamma-ray energy spectra within a factor of approximately five, with those obtained from the more detailed three-dimensional procedure. The three-dimensional analysis gives definitive results. However, when analyses are required to evaluate the performance of the neutral beam injectors as a function of design changes or to establish shielding requirements for the injectors or personnel working in the vicinity, then the two-dimensional procedure described here is an efficient analytic tool.

REFERENCES

1. L. C. Pittenger, R. R. Stone, L. E. Valby, and L. R. Pedrotti, "A Neutral Beam Injection System for the Tokamak Fusion Test Reactor", Proceedings of the Seventh Symposium on Engineering Problems of Fusion Research, Knoxville, TN, October 25-28, 1977, Vol. I, pp. 555-559.

2. M. B. Emmett, "The MORSE Monte Carlo Radiation Transport System," ORNL-4972, Oak Ridge National Laboratory (1975).

3. W. A. Rhoades and F. R. Mynatt, "The DOT III Two-Dimensional Discrete Ordinates Code," ORNL/TM-4280, Oak Ridge National Laboratory (1973).

4. Lawrence R. Pedrotti, "The Tokamak Fusion Test Reactor Neutral Beam Injection System Vacuum Chamber," Proceedings of the Seventh Symposium on Engineering Problems of Fusion Research, Knoxville, TN, October 25-28, 1977, Vol. II, pp. 1001-1006.

5. Lawrence E. Valby, "Cryopumping System for the TFTR Neutral Beam Injectors," Proceedings of the Seventh Symposium on Engineering Problems on Fusion Research, Knoxville, TN, October 25-28, 1977, Vol. II, pp. 1040-1044.

6. Roger R. Stone and James M. Hanghian, "The Design of the Calorimeter and Beam Dump for the TFTR Prototype Neutral Beam Injector," Proceedings of the Seventh Symposium on Engineering Problems on Fusion Research, Knoxville, TN, October 25-28, 1977, Vol. II, pp. 1425-1430.

7. Engineering drawings were provided by Ebasco Services, Inc. and the Lawrence Livermore Laboratory.

8. B. Pritchard, Princeton Plasma Physics Laboratory, private communication.

References (Cont'd)

9. M. B. Emmett, C. E. Burgart, T. J. Hoffman, "DOMINO, A General Purpose Code for Coupling Discrete Ordinates and Monte Carlo Radiation Transport Calculations," ORNL-4853, Oak Ridge National Laboratory (1973).

10. R. L. Childs, Oak Ridge National Laboratory, private communication.

11. W. E. Ford, III, R. T. Santoro, R. W. Roussin, and D. M. Plaster, "Modification Number One to the Coupled 100n-21γ Cross-Section Library for EPR Calculations," ORNL/TM-5249, Oak Ridge National Laboratory (1976).

12. M. A. Abdou, C. W. Maynard, R. Q. Wright, "MACK - A Computer Program to Calculate Neutron Energy Release Parameters (Fluence-to-Kerma Factors) and Multigroups Neutron Reaction Cross Sections from Nuclear Data in ENDF Format," ORNL/TM-3994, Oak Ridge National Laboratory (1973).

13. N. M. Greene et al., "AMPX: A Modular Code System for Generating Coupled Multigroup Neutron-Gamma Libraries from ENDF/B," ORNL/TM-3706, Oak Ridge National Laboratory (1976).

THIS PAGE

WAS INTENTIONALLY

LEFT BLANK

ORNL/TM-6354
Dist. Category UC-20d

Internal Distribution

1. L. S. Abbott
2. F. S. Alsmiller
3-12. R. G. Alsmiller, Jr.
13. J. Barish
14. J. M. Barnes
15. L. A. Berry
16. T. A. Gabriel
17. H. Goldstein (Consultant)
18-27. R. A. Lillie
28. F. C. Maienschein
29-38. R. T. Santoro
39. Y. Seki
40. D. Steiner
41. P. Greebler (Consultant)
42. W. B. Loewenstein (Consultant)
43. R. E. Uhrig (Consultant)
44. R. Wilson (Consultant)
45-46. Central Research Library
47. ORNL Y-12 Technical Library
Document Reference Section
48. Laboratory Records Department
49. ORNL Patent Office
50. Laboratory Records - RC

External Distribution

51. F. E. Coffman, Chief, Systems and Applications Studies Branch, Office of Fusion Energy, U.S. Dept. of Energy, Washington, D.C. 20545
52. W. Cooper, Lawrence Berkeley Laboratory, Neutral Beam Group, Berkeley, CA 94720
53. J. N. Grace, Office of Fusion Energy, U.S. Dept. of Energy, Washington, D.C. 20545
54. C. R. Head, Office of Fusion Energy, G-234, U.S. Dept. of Energy, Washington, D.C. 20545
55. H. W. Hendel, Plasma Physics Laboratory, Princeton University, P. O. Box 451, Princeton, NJ 08540
56. R. Hensler, Ebasco Services, Inc., 2 Rector St., NY, NY 10006
57. H. J. Howe, Jr., Plasma Physics Laboratory, Princeton University, P.O. Box 451, Princeton, NJ 08540
58. R. Little, Plasma Physics Laboratory, Princeton University, P.O. Box 451, Princeton, NJ 08540
59. K. G. Moses, Office of Fusion Energy, U.S. Dept. of Energy, Washington, D.C. 20545
60. L. C. Pittenger, Lawrence Livermore Laboratory, P.O. Box 808-L383, Livermore, CA 94550
61. L. K. Price, Office of Fusion Energy, U.S. Dept. of Energy, Washington, D.C. 20545
62. W. G. Price, Plasma Physics Laboratory, Princeton University, P.O. Box 451, Princeton, NJ 08540
63. B. Pritchard, Plasma Physics Laboratory, Princeton University, P.O. Box 451, Princeton, NJ 08540
64. P. J. Reardon, Plasma Physics Laboratory, Princeton University, P.O. Box 451, Princeton, NJ 08540
65. G. Sheffield, Plasma Physics Laboratory, Princeton University, P.O. Box 451, Princeton, NJ 08540

External Distribution (Cont'd)

66. E. Stern, Plasma Physics Laboratory, Princeton University, P.O. Box 451, Princeton, NJ 08540
67. K. Wright, Plasma Physics Laboratory, Princeton University, P.O. Box 451, Princeton, NJ 08540
68. K. Young, Plasma Physics Laboratory, Princeton University, P.O. Box 451, Princeton, NJ 08540

69-213. Given distribution as shown in TID-4500, Magnetic Fusion Energy (Distribution Category UC-20d: Fusion Systems)